Structural characterization of SARS-CoV-2 dimeric ORF9b reveals potential fold-switching trigger mechanism

Xiyue Jin[1,2], Xue Sun[3,4], Yan Chai[2], Yu Bai[2,5], Ying Li[2,5], Tianjiao Hao[2,5], Jianxun Qi[2,5], Hao Song[5,6*], Catherine CL Wong[3,4,7,8*] & George F. Gao[1,2,5,6*]

[1]School of Life Sciences, Division of Life Sciences and Medicine, University of Science and Technology of China, Hefei 230027, China;
[2]CAS Key Laboratory of Pathogen Microbiology and Immunology, Institute of Microbiology, Chinese Academy of Sciences, Beijing 100101, China;
[3]Peking University First Hospital, Peking University, Beijing 100034, China;
[4]Center for Precision Medicine Multi-Omics Research, Peking University Health Science Center, Peking University, Beijing 100191, China;
[5]University of Chinese Academy of Sciences, Beijing 100049, China;
[6]Research Network of Immunity and Health (RNIH), Beijing Institutes of Life Science, Chinese Academy of Sciences, Beijing 100101, China;
[7]Peking-Tsinghua Center for Life Sciences, Peking University, Beijing 100871, China;
[8]School of Basic Medical Sciences, Peking University Health Science Center, Peking University, Beijing 100191, China

The constant emergence of severe acute respiratory syndrome coronavirus 2 (SARS-CoV-2) variants indicates the evolution and adaptation of the virus. Enhanced innate immune evasion through increased expression of viral antagonist proteins, including ORF9b, contributes to the improved transmission of the Alpha variant; hence, more attention should be paid to these viral proteins. ORF9b is an accessory protein that suppresses innate immunity via a monomer conformation by binding to Tom70. Here, we solved the dimeric structure of SARS-CoV-2 ORF9b with a long hydrophobic tunnel containing a lipid molecule that is crucial for the dimeric conformation and determined the specific lipid ligands as monoglycerides by conducting a liquid chromatography with tandem mass spectrometry analysis, suggesting an important role in the viral life cycle. Notably, a long intertwined loop accessible for host factor binding was observed in the structure. Eight phosphorylated residues in ORF9b were identified, and residues S50 and S53 were found to contribute to the stabilization of dimeric ORF9b. Additionally, we proposed a model of multifunctional ORF9b with a distinct conformation, suggesting that ORF9b is a fold-switching protein, while both lipids and phosphorylation contribute to the switching. Specifically, the ORF9b monomer interacts with Tom70 to suppress the innate immune response, whereas the ORF9b dimer binds to the membrane involving mature virion assembly. Our results provide a better understanding of the multiple functions of ORF9b.

SARS-CoV-2, ORF9b, immune escape, viral antagonist, membrane association, fold switch, lipid binding

INTRODUCTION

The ongoing coronavirus disease 2019 (COVID-19) pandemic, caused by the severe acute respiratory syndrome coronavirus 2 (SARS-CoV-2) (Bai et al., 2022; Lu et al., 2020; Wu et al., 2020; Zhu et al., 2020), seemed to be endless with continuous evolution in the foreseeing future. The constant emergence of SARS-CoV-2 variants of concern (VOCs) indicates viral evolution and adaptation. Much attention has been paid to the characterization of spike changes

---

in VOCs, which are associated with altered transmissibility and extensive immune escape (McCallum et al., 2021; Zhang et al., 2021), while other mutations that occur outside the spike region in circulating variants are ignored. The SARS-CoV-2 lineage B.1.1.7, also known as the Alpha VOC, more effectively suppresses the innate immune responses, resulting in high transmissibility owing to the massively enhanced expression of N, ORF9b, and ORF6, all of which are innate immune antagonists (Thorne et al., 2022; Yang et al., 2021). For the comparable mutations that present in the Delta and Omicron N/ORF9b Kozak regions, variations outside the spike region also play a key role in the SARS-CoV-2 viral evolution (Thorne et al., 2022). In addition, anti-ORF9b antibodies have been identified in the sera of SARS-CoV and SARS-CoV-2 patients (Jiang et al., 2020a; Li et al., 2021; Qiu et al., 2005), indicating the significance of ORF9b in confirming the diagnosis and eliciting an immune response to the virus. Thus, understanding the molecular mechanism of ORF9b is crucial, presumably contributing to a better understanding of virus evolution and exploring the key targets of treatment against COVID-19.

The accessory protein ORF9b is translated as an alternative open reading frame (ORF) within the N gene via a leaky scanning mechanism (Xu et al., 2009). SARS-CoV ORF9b shows a 72.45% sequence identity with SARS-CoV-2 ORF9b. SARS-CoV ORF9b revealed a homodimer β-rich structure with a long hydrophobic lipid-binding tunnel, suggesting its role in membrane binding and mature virion assembly (Meier et al., 2006; Xu et al., 2009). Intriguingly, recent studies have demonstrated that SARS-CoV-2 ORF9b suppresses innate immunity by binding to Tom70, consequently undermining the ability of Tom70 to bind with Hsp90/TBK1/IRF3 and ultimately suppress the production of type I interferons (IFN-Is) (Brandherm et al., 2021; Gao et al., 2021; Gordon et al., 2020a; Jiang et al., 2020b; Liu et al., 2010); therefore, ORF9b is a viral antagonist of host innate immunity. Complex structures showed that ORF9b takes on a new fold when it binds to Tom70, with a part of it switching to a long α-helix formation (Gao et al., 2021; Gordon et al., 2020a).

Here, we identified the dimeric structures of SARS-CoV-2 ORF9b using two kinds of preparations, in vitro expressed soluble and refolded forms, which showed a long hydrophobic tunnel containing a lipid that is crucial for the dimeric conformation; we also determined that the lipid ligands in ORF9b expressed in different expression systems are the same using liquid chromatography with tandem mass spectrometry (LC-MS/MS) analysis, indicating their critical role in the virus life cycle. The phosphorylation sites of ORF9b were analyzed by LC-MS/MS, and eight phosphorylated residues were identified. Additionally, we proposed a model of multifunctional ORF9b with distinct structures, suggesting that ORF9b is a fold-switching protein. Specifically, the

ORF9b monomer interacts with the mitochondrial outer membrane receptor Tom70 to suppress the innate immune response, whereas the ORF9b dimer conformation binds to the membrane involving mature virion assembly. To the best of our knowledge, ORF9b is the first fold-switching protein (Porter and Looger, 2018) of the SARS-CoV-2 with diverse functions, implicating the cunning and economical mechanism of this virus with this delicate protein.

RESULTS

Crystal structure of SARS-CoV-2 ORF9b dimer

The soluble form of SARS-CoV-2 ORF9b protein was obtained in *Escherichia coli* (Figure 1A). The sedimentation-velocity analytical ultracentrifugation assay confirmed that ORF9b proteins exist as homodimers in solution (Figure 1B). Then, the dimeric structure of SARS-CoV-2 ORF9b was determined by X-ray crystallography at 2.95 Å resolution (Table 1 for details) and by molecular replacement using the SARS-CoV ORF9b structure (PDB ID code 2CME) as the search model (Meier et al., 2006). Two dimeric ORF9b molecules were found in one asymmetric unit, one with chains A and B and the other with chains C and D (Figure S1 in Supporting Information). The dimer formed by chains C and D, being more integral, was used for analysis in this study. The crystal structure showed that ORF9b is a two-fold symmetric dimer constructed from two adjacent twisted β-strands, resembling an aircraft (Figure 1C). Each ORF9b protomer consisted of eight winding β-strands (Figure 1C). Extensive interactions, involving both hydrophobic and polar interactions, bury a surface area over 1,470 Å^2 (calculated using the proximal isovelocity surface area (PISA) method) between the two protomers (Figure 1D). In particular, the dimeric ORF9b structure is constructed with 29 hydrogen bonds between two protomers and two salt bridges formed by residue R58 of one protomer and residue E90 of another protomer. The intermolecular bonds between two protomers are contributed by the β2 of one protomer and β2 of the other, the residues of one subunit's β5 and the other subunit's β8, and the interaction between β8 of one monomer and β5 of the other, involving 31 residues of the two subunits (Figure 1E–G). The two salt bridges formed between residue R58 of one monomer's β5 and residue E90 of the other's β8 contribute to the stabilization of the dimer's two wings. Interestingly, residue R58 of chain C also interacts with the amidogen of residue R25 of chain D (Figure 1F), contributing to the stabilization of the β2–β3 loop of chain D. Another polar contact between two nonadjacent secondary structures is formed by residue N55 of chain C and residue R47 of chain D (Figure 1F).

The SARS-CoV-2 ORF9b structure is similar to that of SARS-CoV ORF9b, with a root-mean-square deviation
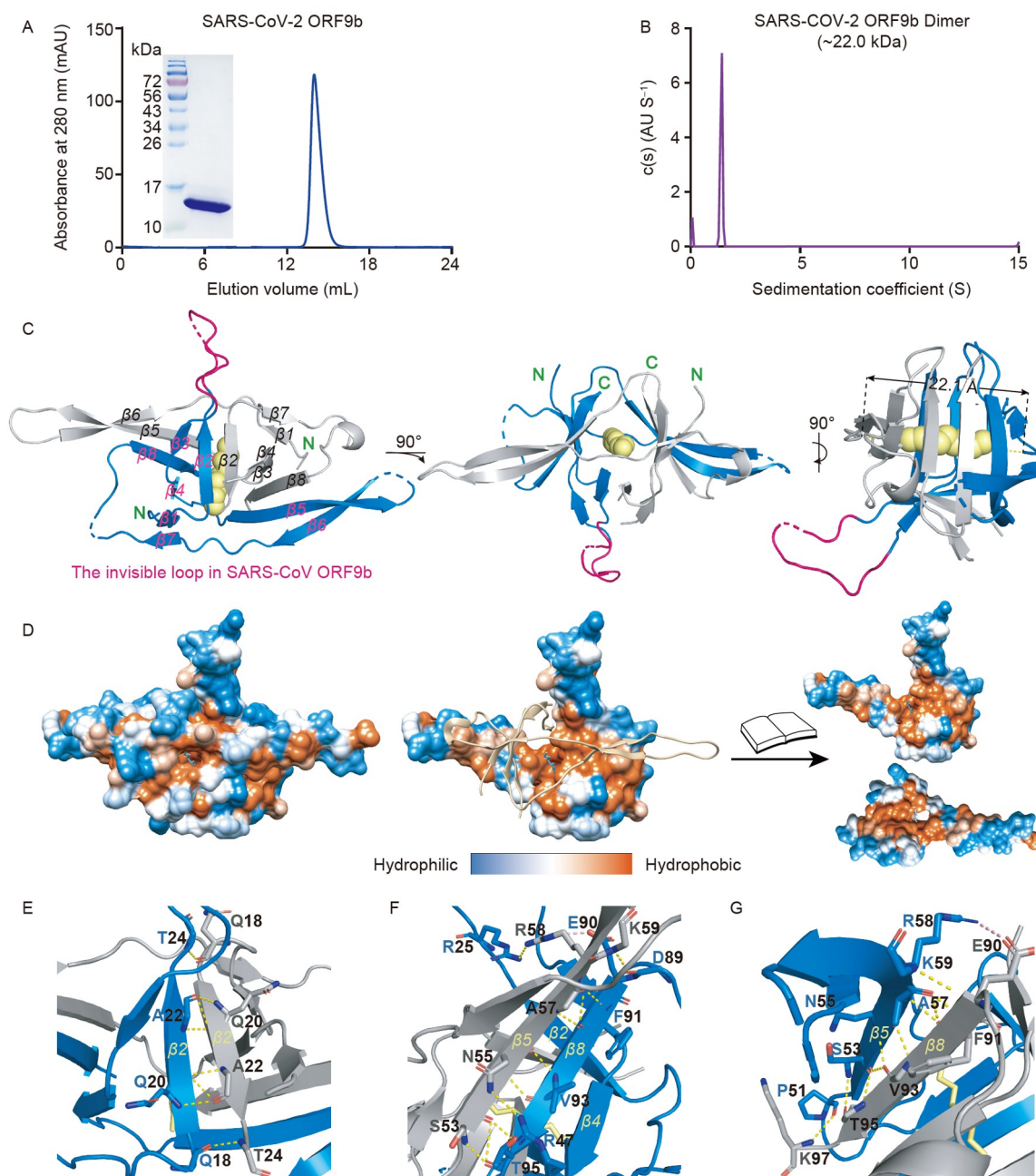
Figure 1 Crystal structure of SARS-CoV-2 ORF9b dimer. A, Analytical gel filtration of SARS-CoV-2 ORF9b with a Superdex™75 10/300 GL column. B, Ultracentrifugation sedimentation profiles of SARS-CoV-2 ORF9b. C, Cartoon representation of the SARS-CoV-2 ORF9b dimeric structure, with one subunit in gray color and another in marine. Three orthogonal views were presented. The invisible loop in the SARS-CoV ORF9b structure is in hot pink color. The lipid ligands shown as spheres are in pale yellow color. The secondary structural elements are labeled in the upper image, *β1* 13–15, *β2* 19–23, *β3* 40–42, *β4* 44–48, *β5* 53–62, *β6* 67–73, *β7* 78–80, and *β8* 90–96. The N termini are labeled in green. D, Hydrophobic properties of the SARS-CoV-2 ORF9b dimer. Molecular surfaces were colored according to their hydrophobicity, with blue, white, and orange corresponding to the most hydrophilic, neutral, and hydrophobic patches, respectively. E–G, Detailed view of dimeric SARS-CoV-2 ORF9b interface. The residues involved in dimer formation are labelled and shown as sticks. The hydrogen bonds are indicated by yellow dashed lines, whereas the salt bridges are indicated by pink lines.

(RMSD) of 0.976 Å. Despite their overall resemblance, our crystal structure reveals valuable new information about a flexible loop (residues 24–39, namely, the *β2–β3* loop) that is not visible in previous structures. Notably, we can observe the *β2–β3* loop (Figure 1C and Figure S1 in Supporting Information) in one monomer, which is invisible in SARS-CoV ORF9b, as well as in another released SARS-CoV-2

ORF9b (PDB ID code 6Z4U) structure. The *β2–β3* loop in chain D is stabilized owing to its interaction with the *β2* and *β3* strands of chain B in the other dimer (Figure S1A in Supporting Information). The *β2–β3* loop is the longest loop in the ORF9b structure. This large flexible loop extends outward and resembles a tentacle ready to contact with other proteins, implying a biological role.

Table 1 Crystallographic data collection and refinement statistics for SARS-CoV-2 ORF9b[a]

	ORF9b_soluble	ORF9b_refolded
Data collection		
Space group	P 32 2 1	P 32 2 1
Cell dimensions		
a, b, c (Å)	73.58, 73.58, 175.62	73.67, 73.67, 176.68
α, β, γ (°)	90.00, 90.00, 120.00	90.00, 90.00, 120.00
Resolution (Å)	50.00–2.95 (3.06–2.95)*	50.00–3.00 (3.11–3.00)*
R_{merge}	0.061 (0.671)	0.065 (1.392)
$I / \sigma I$	34.357 (4.569)	46.615 (3.000)
Completeness (%)	99.8 (100.0)	100.0 (100.0)
Redundancy	17.1 (16.2)	19.1 (19.5)
Refinement		
Resolution (Å)	31.15–2.95	28.29–3.01
No. reflections	12059	11230
R_{work} / R_{free}	0.2657 / 0.2892	0.2449 / 0.3119
No. atoms		
Protein	2315	2487
Ligand/ion	17	16
Water	0	0
B-factors		
Protein	43.99	42.28
Ligand/ion	30.06	12.34
Water	–	–
R.m.s. deviations		
Bond lengths (Å)	0.005	0.003
Bond angles (°)	0.733	0.709
Ramachandran plot		
Favored (%)	95.65	95.42
Allowed (%)	4.35	4.58
Outliers (%)	0.00	0.00

a) * Values in parentheses are for highest-resolution shell.

The electrostatic surface potential maps of SARS-CoV-2 ORF9b were compared with those of SARS-CoV ORF9b. Previously, two surfaces with a distinct polarized distribution of surface electrostatics from SARS-CoV ORF9b were observed, with one surface of the molecule being negatively charged (top surface) and the other being positively charged (bottom surface) (Figure S2B in Supporting Information) (Meier et al., 2006). A positively charged surface has been proposed to contribute to the membrane association (Meier et al., 2006). For SARS-CoV-2 ORF9b, although the bottom surface is similar to that of SARS-CoV ORF9b, the top surface exhibits a composite surface containing both positively and negatively charged regions, suggesting the evolution of the virus within the host (Figure S2A in Supporting Information). Importantly, the intertwined *β2–β3* loop observed in our structure is located at the top surface, which is

beneficial for interacting with host factors.

Contribution of S50 and S53 in the dimerization and phosphorylation of ORF9b

Residue S53 was previously identified as a key residue for binding Tom70 (Brandherm et al., 2021; Gao et al., 2021; Thorne et al., 2022). S50 and S53 were highly conserved (Figure 2A), and deletion of these residues (S50A and S53A) disrupted the protein folding, resulting in a soluble aggregate (Figure 2B). In addition, mutation of these residues greatly reduced the dimeric ORF9b, and the mutants were less stable (Figure 2B), suggesting that they are important in forming dimeric ORF9b. Protein phosphorylation is a key physiological regulatory mechanism, and phosphorylation of the ORF9b residue S53 inhibits ORF9b binding to hTom70 (Brandherm et al., 2021; Thorne et al., 2022). Mammalian cell-expressed ORF9b proteins were purified to identify the phosphorylated residues via LC-MS/MS analysis. Eight phosphorylated residues (Y42, S50, S53, S63, T72, T83, T84, and T95) were observed (Figure 2C).

Importance of lipids in the formation of dimeric ORF9b

Similar to SARS-CoV ORF9b, the *β* sheets of SARS-CoV-2 ORF9b form a 22.1 Å long hydrophobic cavity similar to an aircraft's cabin (Figure 1C and 1D). The cavity accommodates a lipid ligand containing nine carbon atoms, according to the experimentally phased electron density, lined by conserved hydrophobic residues (Figure 2A), suggesting the physiological significance of this hydrophobic cavity along with the lipid inside. To determine whether dimeric ORF9b could be obtained without lipids, the inclusion body was purified, and the refolded ORF9b proteins were obtained following an *in vitro* refolding method. The crystal structure was then resolved at 3 Å resolution (Table 1 for details). Surprisingly, the refolded ORF9b structure is similar to the soluble ORF9b structure with lipids in the cavity (Figure 3A), suggesting the significant importance of the lipid in forming the dimeric structure. To identify the specific lipid bound in the "cabin," MS analysis was carried out. The lipid ligands in SARS-CoV ORF9b, SARS-CoV-2 ORF9b soluble, and SARS-CoV-2 ORF9b refolded protein samples were analyzed, using GST proteins as a negative control. The SARS-CoV-2 ORF9b expression in 293T mammalian cells was also evaluated to determine whether different expression methods have an effect on the ligand. The results were inspiring. Even in diverse expression systems, the lipid exhibited good specificity (Figure 3C), implying that the ligand plays a key role in the virus life cycle. Results of the MS analysis of the extracted ligand molecule from soluble SARS-CoV-2 ORF9b and refolded ORF9b showed that the ligand was 1-octadecanoyl-rac-glycerol (MG 18:0, $C_{21}H_{42}O_4$),
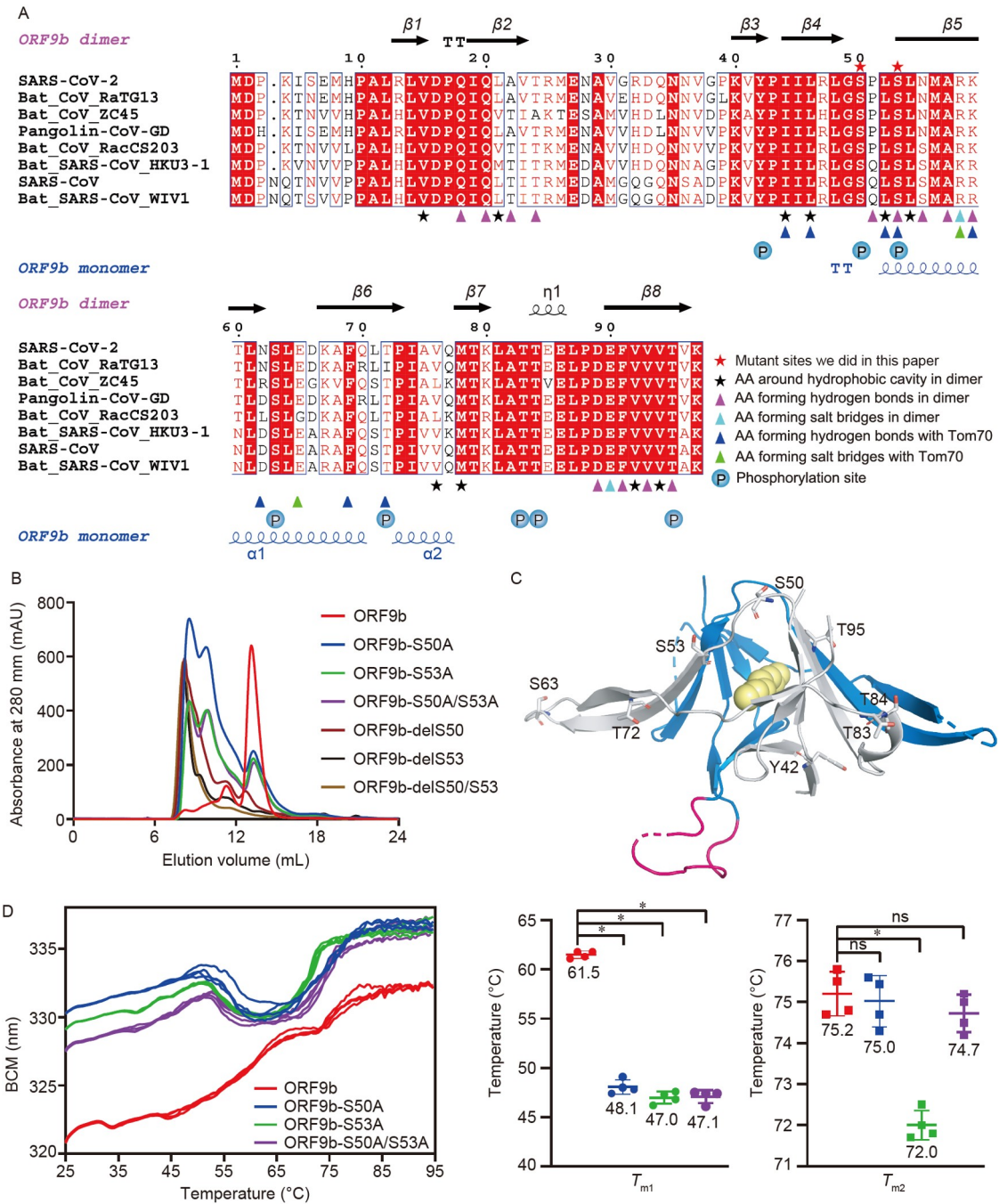
Figure 2   Importance of S50 and S53 in the formation and phosphorylation of dimeric ORF9b. A, Structure-guided sequence alignment of SARS-CoV-2 ORF9b with other CoV ORF9b. Multiple sequence alignment of SARS-CoV-2 ORF9b between several SARS-CoV-like coronavirus and SARS-CoV-2 like coronavirus. SARS-CoV-2 ORF9b has two different conformations: a dimeric structure rich in β strands shown above the sequence alignment are colored in black, while a monomer partially forms the primary α-helix when bound to Tom70 (colored in blue) located below the sequence alignment. The key residues are labeled using the corresponding symbol. B, Analytical gel-filtration chromatography of SARS-CoV-2 ORF9b and ORF9b mutants was performed using a Superdex^{TM}75 10/300 GL column. C, ORF9b phosphorylation sites. The phosphorylated residues are indicated as ligands. D, Thermal stability assay for SARS-CoV-2 soluble ORF9b and three mutants, measured by fluorescence, whose melting temperatures (T_m) are shown as an indicator of protein domain unfolding. The concentrations of the three proteins were the same (3.5 mg mL^{-1}).

similar to the ligand found in SARS-CoV ORF9b, named 1-hexadecanoyl-sn-glycerol (MG 16:0, $C_{19}H_{38}O_4$) (Figure 3D). Remarkably, both molecules were identified in SARS-CoV-2 ORF9b mammalian samples, indicating that the ORF9b from SARS-CoV and SARS-CoV-2 has conserved and broad li-

pid-binding properties for dimer formation. Further thermostability assays indeed showed that refolded ORF9b was less stable than the soluble ORF9b (Figure 3B), presumably because of the different purification methods used. In addition, the small amounts of lipids present during *in vitro* re-
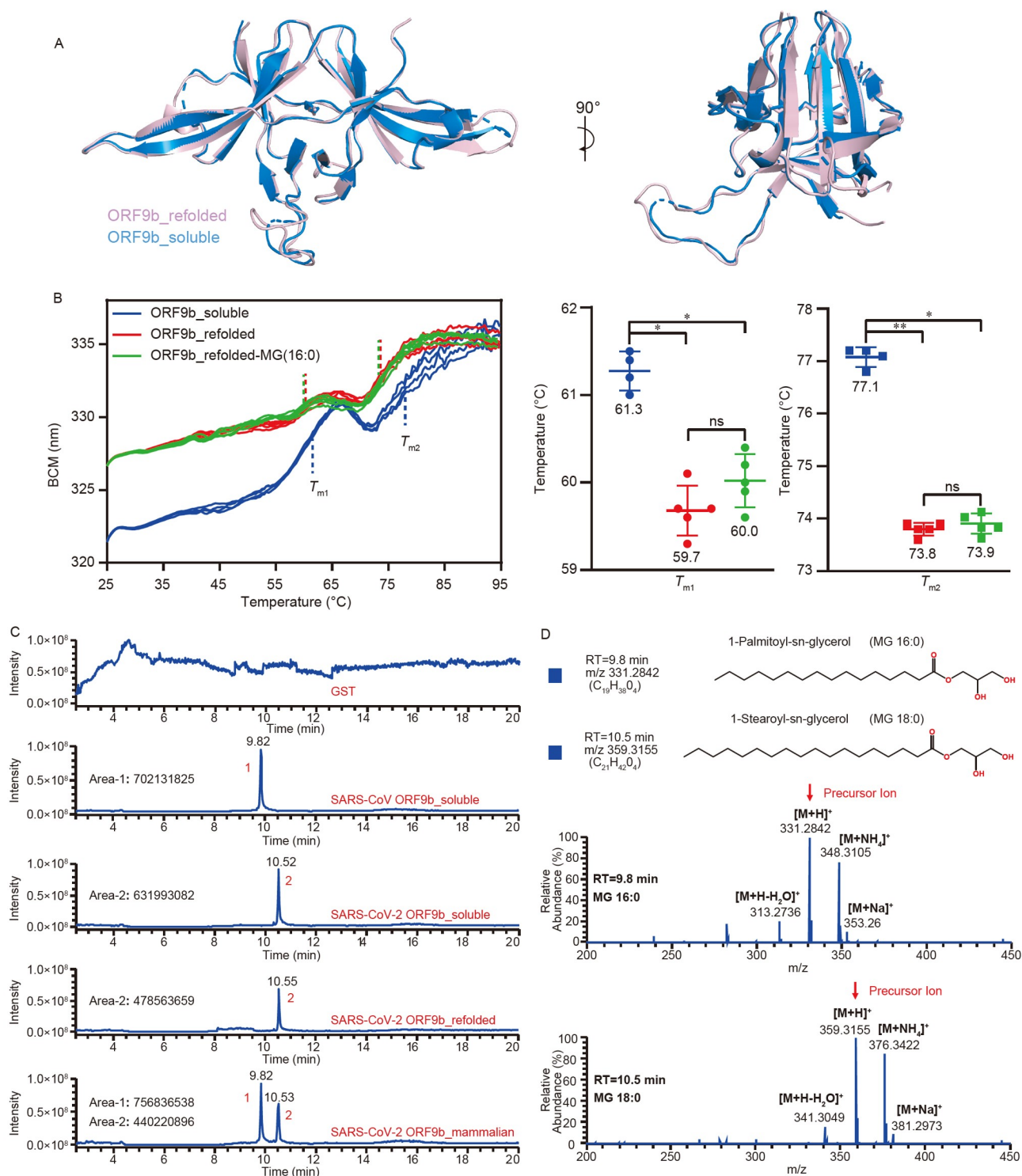
Figure 3 Importance of lipid molecule in the central hydrophobic cavity for dimer stability. A, Superimposition of the SARS-CoV-2-soluble ORF9b dimeric structure with SARS-CoV-2-refolded ORF9b conformation. B, The thermal stability assay for SARS-CoV-2-soluble ORF9b and SARS-CoV-2-refolded ORF9b as well as SARS-CoV-2-refolded ORF9b with MG (16:0), measured by fluorescence, and the melting temperatures (T_m) are shown as indicators of protein domain unfolding. Soluble ORF9b showed a higher T_m than the refolded ORF9b, suggesting that the former conformation was more stable. The T_m of SARS-CoV-2-refolded ORF9b and that of SARS-CoV-2-refolded ORF9b, with MG (16:0) showing the absence of statistical difference. The concentrations of the three proteins were the same (4.5 mg mL^{-1}). C, HPLC chromatograms of SARS-CoV-soluble ORF9b, SARS-CoV-2-soluble ORF9b, SARS-CoV-2-refolded ORF9b, SARS-CoV-2 ORF9b mammalian, and GST as contrast, showing two prominent peaks at specific retention times. D, Mass spectrum of the ligand molecule of SARS-CoV-soluble ORF9b, SARS-CoV-2-soluble ORF9b, SARS-CoV-2-refolded ORF9b, and SARS-CoV-2 ORF9b mammalian, corresponding to the two peaks from (C). At an RT of 9.8 min, the mass spectrum suggested that the ligand was MG (16:0), which is also known as 1-palmitoyl-sn-glycerol or 1-hexadecanoyl-sn-glycerol ($C_{19}H_{38}O_4$). At an RT of 10.5 min, the mass spectrum suggested that the ligand was MG (18:0), also named 1-stearoyl-sn-glycerol or 1-octadecanoyl-sn-glycerol ($C_{21}H_{42}O_4$).

folding assisted the optimization of protein solubility. An experiment was conducted to resolve this issue. Lipids were added during the refolding experiment to observe their contribution to protein stability. Owing to its hydrophobicity, DMSO was used to dissolve the MG (16:0). The volume ratio between the lipid and protein was 1/500, and the molar ratio was 30/1. After co-incubation for 4 h at 4°C, the protein stability was evaluated using thermal stability assay, but no statistical difference was found; this finding indicated that excess lipids cannot contribute to the protein stability using this method (Figure 3B).

Fold switching from monomer to dimer

Interestingly, ORF9b possesses two radically different conformations (Figure 4). The ORF9b showed a β-strand-rich

homodimer structure with a hydrophobic tunnel containing a lipid, suggesting its role in membrane binding (Meier et al., 2006) and mature virion assembly (Xu et al., 2009). Confocal experiments of ORF9b showed its cytosolic distribution and plasma membrane localization (Lee et al., 2021). In addition, ORF9b monomer interacts with the human mitochondrial outer membrane receptor Tom70, leading to the modulation of interferon signaling and reduction in mitochondrial import efficiency (Brandherm et al., 2021; Gordon et al., 2020a; Jiang et al., 2020b). When binding to Tom70, ORF9b adopts a different fold, part of which switches to a long α-helix (Gao et al., 2021; Gordon et al., 2020a). Briefly, between residues 43 and 78, β4 folds into a loop, whereas β5, β6, and half of β7 along with the two internal loops transform into a long α-helix (Figure 4B). This region plays an important role in the formation of dimeric
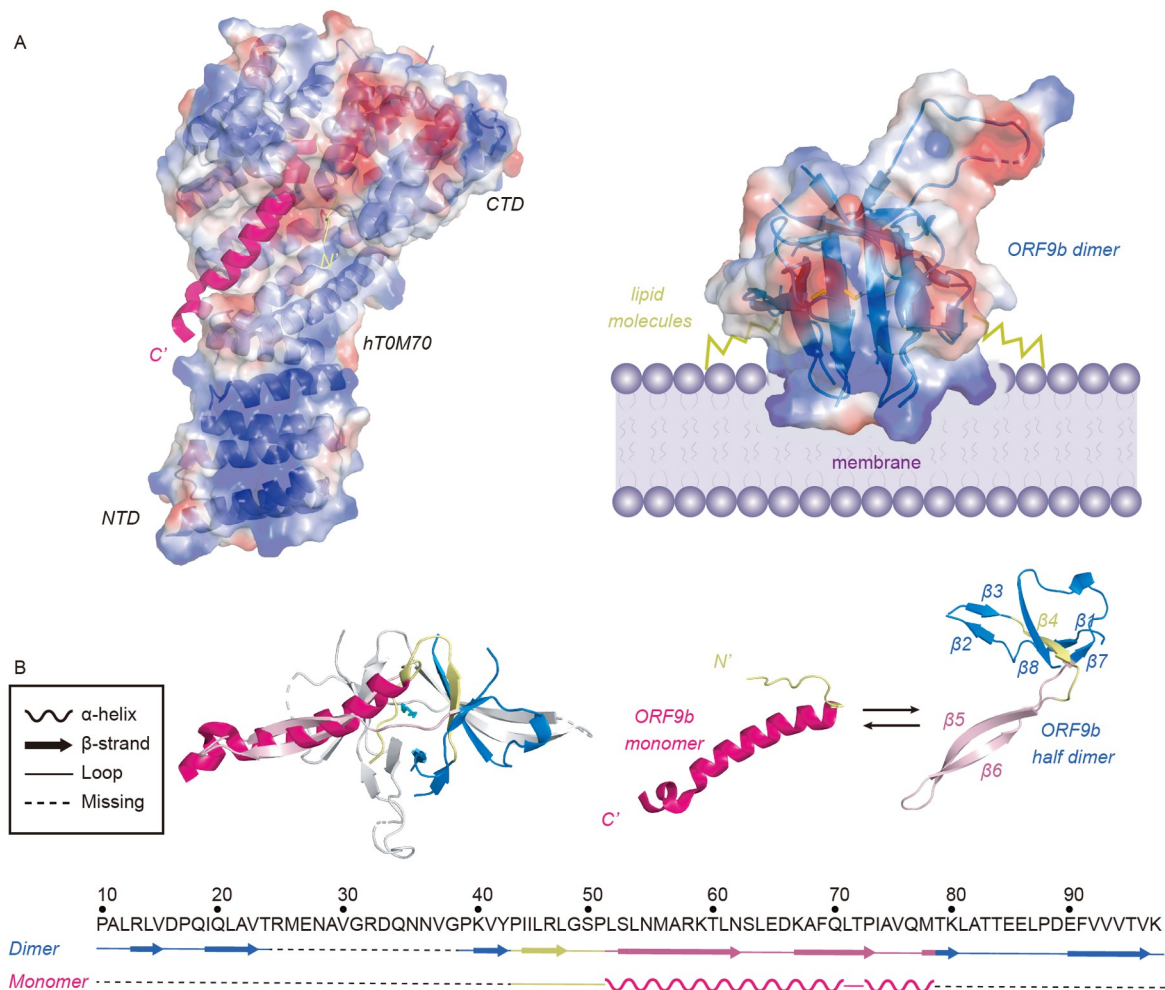

Figure 4   Structure comparison of ORF9b fold switching from monomer to dimer. A, Left, cartoon representation of SARS-CoV-2 ORF9b shown in hot pink with Tom70 of electrostatic potential surface view (PDB ID code 7DHG). The SARS-CoV-2 ORF9b is accommodated at the CTD-pocket of Tom70, which is negatively charged, while the NTD-pocket is positively charged. Right, proposed mode of SARS-CoV-2 ORF9b membrane binding (electrostatic potential surface view represented as in Figure S2 in Supporting Information). The positively charged side of ORF9b could interact with the membrane, while the lipid accommodates at the hydrophobic cavity. B, Cartoon models of the dimeric SARS-CoV-2 ORF9b structure and the monomer conformation when bound to Tom70. The monomer SARS-CoV-2 ORF9b consists of a loop (pale yellow) and a helix (hot pink), while the corresponding parts in the dimeric structure are β strands (pale yellow) and loops (pink); the rest of subunit is colored in marine.

ORF9b and in monomer binding with Tom70. Between residues 43 and 78, residues I44/L46/L52/L54/V76/M78 contributed to the hydrophobic cavity of dimeric ORF9b. Residues P51/S53/S55/A57/K59/R58 are involved in the formation of hydrogen bonds and salt bridges in dimeric ORF9b. Residues I44/L46/L52/S53/R58/K59/N62/E65/F69/T72 participate in the formation of hydrogen bonds and salt bridges between ORF9b and TOM70 (Figure 2A). ORF9b residues 43–64, which are buried in the hTom70 CTD-binding pocket, are more conserved compared with residues 65–78, which are exposed (Figure 2). Sequence alignment revealed that the residues that interact with Tom70 are less conserved than those involved in dimer formation (Figure 2A), which suggests the continuous evolution and adaptation of the virus to the host immune system. Of the 15 residues involved in the formation of dimeric ORF9b, only six (A22/T24/P51/N55/R58/K59) were variable, while the others were highly conserved (Figure 2A). Among the ten residues that interact with TOM70, five (R58/K59/N62/E65/T72) were variable.

Proposed model for multifunctional ORF9b

Previous studies demonstrated that the expression of SARS-CoV-2 ORF9b alone undermines the innate immune response by interacting with Tom70 (Brandherm et al., 2021; Gordon et al., 2020a; Jiang et al., 2020b). Briefly, ORF9b binds to the CTD-pocket of hTom70, allosterically inhibiting the interaction between the NTD-pocket of hTom70 and the EEVD motif of Hsp90, which consequently dampens the formation of the Hsp90/TBK1/IRF3 ternary complex and thus ultimately suppresses the induction of IFN-Is (Brandherm et al., 2021; Gao et al., 2021). Brandherm et al. found that the NTD-pocket of hTom70 binds to chaperone-associated ORF9b, which allows subsequent interactions of ORF9b with the CTD-pocket of Tom70, suggesting the complicated mechanism of ORF9b binding to hTom70 (Brandherm et al., 2021). Moreover, the binding of ORF9b to hTom70 is suppressed by the phosphorylation of the residue S53 of ORF9b (Brandherm et al., 2021; Thorne et al., 2022), suggesting a regulatory mechanism. Previous studies reported that ORF9b interacts with MARK, suggesting that MARK contributes to the phosphorylation of ORF9b (Gordon et al., 2020b). Intriguingly, the expression of MARK kinase is downregulated at the early stage of infection (Bouhaddou et al., 2020), which indicates the immune evasion of cunning viruses such as SARS-CoV-2. In addition to the monomer conformation, ORF9b can form a homodimer with a hydrophobic tunnel containing a lipid that is involved in membrane binding (Meier et al., 2006) and mature virion assembly (Xu et al., 2009). Here, we proposed a model for multifunctional ORF9b with a distinct conformation (Figure 5). After being transcribed in the nucleus and transported to

the cytoplasm, there are two pathways for ORF9b subgenomic RNA (sgRNA). On the one hand, sgRNA is translated into ORF9b protomer protein at the rough endoplasmic reticulum and then transported into the Golgi apparatus via the vesicular transport system, where it completes the β-rich dimeric conformation with lipid binding (Figure 5). On the other hand, sgRNA is transported to the mitochondrial outer membrane and translated into the ORF9b monomer, which could bind to the Tom70 CTD-binding pocket with a partially long-helix conformation, regulating the innate immune system by disrupting the interaction between Tom70 and Hsp90. Both phosphorylation and lipid are critical for the fold-switching process. This "one stone, two birds" strategy regulates the SARS-CoV-2 cunning and economical functional pathway.

DISCUSSION

SARS-CoV-2 causes a dysregulated immune response and delayed IFN expression in patients, which contribute significantly to the viral pathogenesis and COVID-19 consequences (Blanco-Melo et al., 2020). COVID-19 progression follows a "two-stage" pattern. Individuals with mild or asymptomatic COVID-19 are immunosuppressed in the early stages, which allows extensive virus shedding and transmission (Tian et al., 2020). However, the underlying mechanism remains unknown. In the early stages following SARS-CoV-2 infection, there is excessive accumulation of the accessory protein ORF9b, while the IFN-β production is delayed (Bojkova et al., 2020). SARS-CoV-2 ORF9b interacts with Tom70 to suppress the innate immunity (Brandherm et al., 2021; Gao et al., 2021; Gordon et al., 2020a; Jiang et al., 2020b), and phosphorylation of the ORF9b residue S53 inhibits the ORF9b binding to Tom70 (Brandherm et al., 2021; Thorne et al., 2022). Using LC-MS/MS, eight phosphorylated ORF9b residues were identified (Figure 2C). In addition to S50 and S53, residues S63 and T72 are also involved in Tom70 binding (Figure 2C). Whether phosphorylation of ORF9b at other residues also regulates innate immunity requires further study. Residues S50 and S53 also contribute for the stabilization of dimeric ORF9b, providing a promising target for drug development.

The phosphorylated ORF9b is disrupted in performing innate immune suppression (Brandherm et al., 2021; Thorne et al., 2022); this finding corresponds to the report of Bouhaddou's study, which showed that MARK kinase, possibly phosphorylating ORF9b (Gordon et al., 2020b), is downregulated after infection with SARS-CoV-2 (Bouhaddou et al., 2020). This raises the question of how viruses regulate the expression of host kinases. Tom70 is a versatile mitochondrial outer membrane adaptor protein that contributes to the protein trafficking, formation of membrane contact
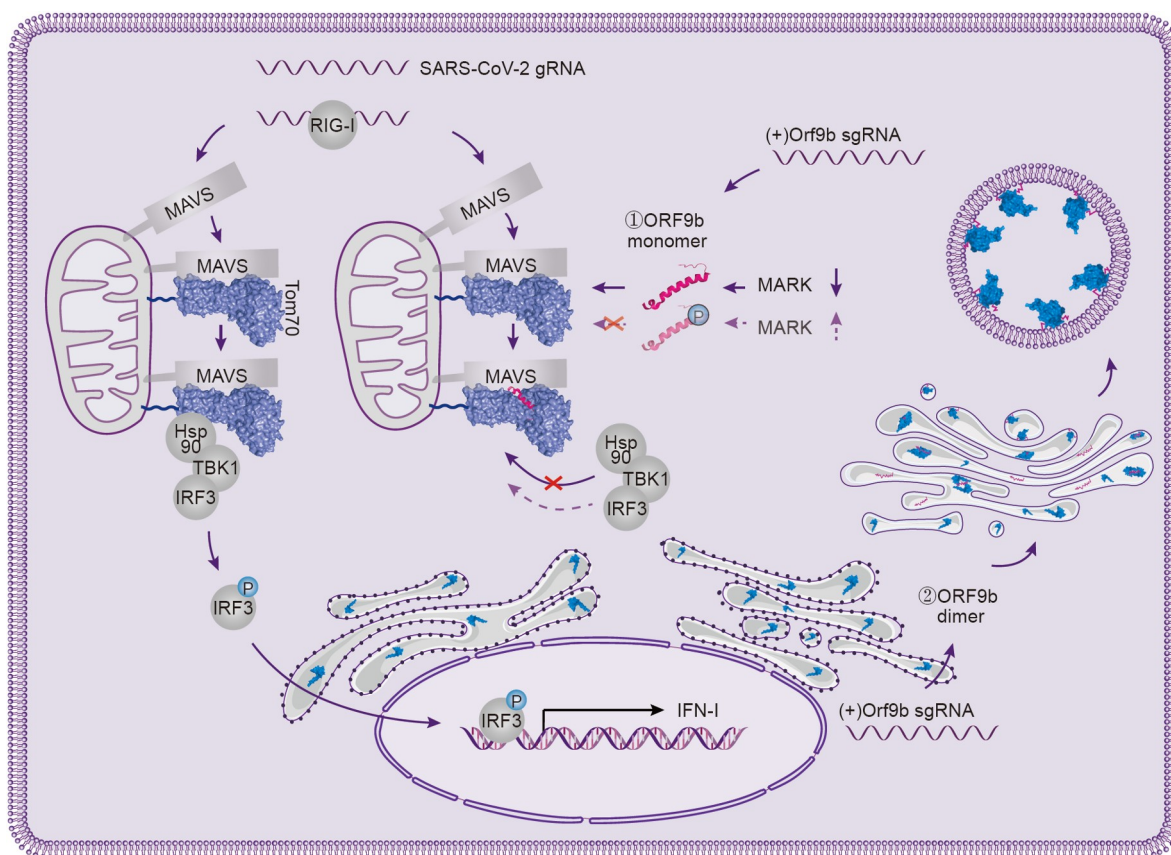
Figure 5 Proposed model for multifunctional ORF9b. Different conformations of SARS-CoV-2 ORF9b have diverse physiological functions. ORF9b could suppress the innate immunity with a monomer conformation bound to Tom70 and contribute to the membrane binding with dimeric structures. Upon SARS-CoV-2 infection, RIG-I binds to the viral RNA and is subsequently associated with mitochondrial antiviral signaling protein (MAVS) on the mitochondrial outer membrane, which triggers MAVS binding to Tom70. The SARS-CoV-2 ORF9b monomer binds to the CTD-pocket of Tom70, allosterically inhibiting the interaction of Hsp90 with the NTD-pocket of Tom70, which consequently dampens the formation of the Hsp90/TBK1/IRF3 ternary complex and ultimately suppresses the induction of type I IFNs. The phosphorylated ORF9b could not dampen the innate immunity owing to its dramatically decreased affinity for Tom70. The expression of MARK is suppressed in the early stages of infection, thus suggesting the compromised innate immunity after infection with SARS-CoV-2. In addition, dimeric ORF9b plays a completely different function in membrane-binding and mature virion assembly. ORF9b sgRNA is translated into a protein at the rough endoplasmic reticulum and then transported into the Golgi apparatus via the vesicular transport system, where it completes the dimeric conformation with lipid binding.

sites, and antiviral signaling (Kreimendahl and Rassow, 2020). The binding of ORF9b to Tom70 produces an additional effect on cellular processes in addition to the innate immunity, such as the transportation of chaperone-bound preproteins (Brandherm et al., 2021). Another study reported that peripheral blood mononuclear cells from COVID-19 patients show mitochondrial dysfunction and reduced mitochondrial respiration with a tendency for glycolysis (Ajaz et al., 2021). Functional regulation of the protein post-translational modification (PTM) of SARS-CoV-2 has also been reported during S glycosylation (Tian et al., 2021).

Anti-dimeric-ORF9b antibodies have been identified in the sera of COVID-19 or SARS-CoV patients (Jiang et al., 2020a; Li et al., 2021; Qiu et al., 2005), indicating that ORF9b plays an important role in the host-virus interactions. In this study, we examined the crystal structure of dimeric SARS-CoV-2 ORF9b; we found that the positively charged bottom surface contributes to the membrane association,

while the top surface of SARS-CoV-2 ORF9b has distinct electrostatic potential properties compared with that of SARS-CoV ORF9b; moreover, this study identified that the intertwined $\beta2$–$\beta3$ loop located at the top surface may contribute to the interactions with host factors or antibody response. However, further research on the ORF9b homodimer involving host-virus interactions and antibody responses is warranted.

Our structure revealed a conserved hydrophobic lipid-binding tunnel similar to SARS-CoV (Meier et al., 2006); the ORF9b binding lipids were identified as 1-octadecanoyl-rac-glycerol (MG 18:0, $C_{21}H_{42}O_4$) and 1-hexadecanoyl-sn-glycerol (MG 16:0, $C_{19}H_{38}O_4$) using LC-MS/MS analysis (Figure 3D). These lipids are monoglycerides produced by various biological processes. Each glycerol molecule forms an ester bond with a fatty acid molecule. They have also been used in food products, emulsifiers, and nanoparticles (Gallarate et al., 2009; Li et al., 2017; Luo et al., 2021; Trivino et

al., 2019; Truzzi et al., 2017). In addition, they are negatively related to the occurrence of bronchial asthma by influencing the glycerophospholipid metabolism (Tian et al., 2017), indicating their critical role in normal metabolic function. ORF9b can be incorporated in both virus-like particles depending on the co-expression of E and M proteins and purified virions (Xu et al., 2009). The lipid-binding properties of ORF9b can be incorporated in the viral or cell membranes. However, further studies are needed to elucidate the underlying mechanisms.

MATERIALS AND METHODS

Protein expression and purification in *E. coli*

The full-length gene of SARS-CoV-2 ORF9b was synthesized and codon optimized into the pET21a vector with a 6×His tag at the N-terminus to determine the expression of *E. coli* at GenScript Company. The plasmid was transformed into *E. coli* strain BL21 (DE3) and then expressed (IPTG, 1 mmol L^{-1} final concentration) at 16°C for 18 h in Luria Broth Base containing ampicillin. The cells were pelleted and resuspended in lysis buffer (20 mmol L^{-1} Tris pH 8.0, 150 mmol L^{-1} NaCl). The cells were lysed by sonication, and the resulting mixture was clarified by centrifugation at 12,000×*g* for 60 min. The supernatant was loaded in a HisTrap HP 5-mL column (GE Healthcare) for purification, while the precipitate required further treatment to obtain the inclusion bodies. After filtration with a 0.22-μm syringe filter, the supernatant was loaded in a HisTrap HP 5-mL column (GE Healthcare). The target protein was eluted using lysis buffer containing 300 mmol L^{-1} imidazole. The eluate was further purified by size exclusion chromatography (SEC) in 20 mmol L^{-1} Tris-HCl pH 8.0 and 150 mmol L^{-1} NaCl using a Superdex^{TM}75 10/300 GL column (GE Healthcare). Mutant plasmids were constructed and expressed in the same manner as for the wild-type protein.

The precipitate was processed using a specific method to obtain the inclusion bodies, as described previously (Li et al., 2005; Song et al., 2016). The inclusion bodies were diluted dropwise in an agitating refolding buffer (100 mmol L^{-1} Tris-HCl pH 8.0, 2 mmol L^{-1} EDTA, 400 mmol L^{-1} L-arginine, 0.5 mmol L^{-1} oxidized glutathione, and 5 mmol L^{-1} reduced glutathione) for at least 12 h at 4°C. The refolding buffer was then concentrated, and the buffer was changed to a lysis buffer using an Amicon® 8400 concentrator. Finally, the protein was purified using SEC and a Superdex^{TM}75 10/300 GL column (GE Healthcare) and the refolded SARS-CoV-2 ORF9b was obtained.

MG (16:0) lipid molecules (Bidepharm, BD305758) were used during the refolding experiment to determine the contribution of lipids to the protein stability. DMSO was used to dissolve the MG (16:0). Then, the lipid and refolded ORF9b

proteins were incubated with each other at a volume ratio of 1:500 and a molar ratio of 30:1. After co-incubation for 4 h at 4°C, the protein stability was assessed by conducting a thermal stability assay.

Protein expression and purification in mammalian cells

The full-length gene of SARS-CoV-2 ORF9b was synthesized and codon optimized into the mammalian expression vector pCAGGS with Twin-Strep-Tag® (Schmidt et al., 2013) following an 8×His tag at the C-terminus to determine its transient expression in 293T cells. The plasmid was transfected into 293T cells using PEI. Three days after transfection, the cells were collected and resuspended in lysis buffer (20 mmol L^{-1} Tris pH 8.0, and 150 mmol L^{-1} NaCl). The cells were lysed via sonication, and the resulting mixture was clarified by centrifugation at 12,000×*g* for 60 min. After filtration with a 0.22-μm syringe filter, the supernatant was loaded in a HisTrap Excel 5-mL column (GE Healthcare) for purification. The target protein was eluted with lysis buffer containing 300 mmol L^{-1} imidazole. The eluate was further purified by SEC in 20 mmol L^{-1} Tris-HCl with a pH of 8.0 and 150 mmol L^{-1} NaCl using a Superdex^{TM}75 10/300 GL column (GE Healthcare).

Crystallization, data collection, and structure determination

The SARS-CoV-2 soluble ORF9b and refolded ORF9b were concentrated to 8 mg mL^{-1} prior to the crystallization trials. An 0.8 μL protein was mixed with 0.8 μL reservoir solution, and the resultant drop was sealed equilibrated against a 100 μL reservoir solution at 18°C using the sitting-drop vapor-diffusion method. The diffraction quality crystals of soluble SARS-CoV-2 ORF-9b protein appeared within 7 days in the reservoir solution containing 2.0 mol L^{-1} ammonium phosphate monobasic and 0.1 mol L^{-1} Tris with a pH of 8; meanwhile, the high-quality crystal of refolded ORF9b grew within 7 days in the reservoir solution containing 0.8 mol L^{-1} sodium phosphate monobasic monohydrate, 0.8 mol L^{-1} potassium phosphate monobasic, and 0.1 mol L^{-1} sodium HEPES with a pH of 7.5. The crystals were transferred into a cryoprotectant (reservoir solution supplemented with 18% ethylene glycol) and soaked for 30–60 s prior to flash freezing in liquid nitrogen. The X-ray diffraction data were collected under cryogenic conditions (100 K) at the Shanghai Synchrotron Radiation Facility beamline BL17U1. The data were indexed, integrated, and scaled using HKL2000 (Otwinowski and Minor, 1997). The structure was determined by molecular replacement using the Phaser MR software (Read, 2001). PDB 2CME was used as the search model. The model was manually built using the Coot software (Emsley and Cowtan, 2004), and the structure

was refined using the PHENIX software (Adams et al., 2010). Information related to the data collection, processing, and refinement statistics are summarized in Table S1 in Supporting Information. The stereochemistry and quality of the structural models were analyzed using Molprobity (Chen et al., 2010), the PISA server (Krissinel and Henrick, 2007), and programs in the CCP4 suite, and were validated using the wwPDB validation server (http://wwpdb-validation.wwpdb.org/validservice). Structural presentations were generated using the PyMOL software (http://www.pymol.org).

Analytical ultracentrifugation

Analytical ultracentrifugation was carried out using Beckman Optima XL-I equipped with an AN-50 Ti rotor with two-channel charcoal-filled centerpieces at 20°C. The protein samples were freshly prepared in a buffer containing 20 mmol L^{-1} Tris pH 8.0 and 150 mmol L^{-1} NaCl at a concentration of A280 = 0.8 before loading. The differential sedimentation coefficients, c(s), frictional coefficients, and molecular weights were calculated using the XL-I data analysis software.

Characterization of the lipid ligand by LC-MS/MS

Approximately 100 μg of purified soluble SARS-CoV ORF9b, soluble SARS-CoV-2 ORF9b, SARS-CoV-2 refolded ORF9b, and SARS-CoV-2 ORF9b mammalian, and GST as a negative control were added to 1,400 μL of extraction buffer (methyl-tert-butyl ether (MTBE): methanol: ddH_2O = 10:2:5, v/v/v) to extract the lipid ligand. The mixtures were vortexed for 60 s and sonicated in a 4°C water bath for 10 min, followed by centrifugation at 3,000 r min^{-1} for 20 min at 4°C. The supernatant (800 μL) was collected in a new tube, and another 500 μL of MTBE was added to the left layer for the second extraction. The pooled organic layers were vacuum centrifuged to dryness and resuspended in 50 μL of methanol (MS grade; Merck, Germany) for LC-MS/MS analysis. Nano-liquid chromatography (EASY-nLC^{TM} 1200 system, Thermo Fisher Scientific, USA) combined with electrospray ionization (ESI)-Q-orbitrap MS (Q-Exactive HF-X, Thermo Fisher Scientific, USA) was employed for lipid characterization. LC separation was performed using a self-packed ReproSil-Pur 120 C_{18} column (7.5 μm (i.d.) × 15 cm (length), 1.9 μm (particle size)) at a flow rate of 200 nL min^{-1}. The column temperature was maintained at 50°C. The elution gradient using mobile phase solvent A (acetonitrile/H_2O (6:4, v/v) with 10 mmol L^{-1} ammonium formate) and solvent B (acetonitrile/2-propanol (1:9, v/v) with 10 mmol L^{-1} ammonium formate) was optimized as follows: 0–1 min = 40% B, 1–13 min = 40% B to 100% B, and 13–20 min = 100% B. The injection volume was 5 μL. The eluted lipids were inlet into MS with a va-

porizer temperature of 350°C and spray voltage of 3,800 V in positive ionization under the all-ion-fragmentation (AIF) mode for MS/MS data acquisition. Mass spectra were scanned from 50 to 750 m/z, and the other MS parameters were set as follows: stepped-normalized collision energy (NCE) = 35 V, resolution = 120,000 FWHM, AGC target = 1e6, maximum injection time = 100 ms, and isolation window = m/z 2.0. Xcalibur 4.1.5 software was utilized to acquire and process the MS and MS/MS data.

LC-MS/MS analysis of protein phosphorylation

To obtain a comprehensive phosphorylation landscape of the ORF9b protein from SARS-CoV-2 virions, the recombinant full-length ORF9b protein expressed in 293T cells was purified. A 50 μg ORF9b protein was precipitated using trichloroacetic acid (Sigma-Aldrich, USA) solution at 4°C for 4 h, centrifuged at 20,000×*g* for 30 min at 4°C, and then washed twice with acetone. The precipitate was dried and resuspended in 40 μL of 8 mol L^{-1} urea (Sigma-Aldrich, USA) (Tris/HCl buffer, pH of 8.5), reduced with 20 mmol L^{-1} Tris-(2-carboxyethyl) phosphine (TCEP, Thermo Fisher Scientific, USA) (Tris/HCl buffer, pH 8.5) at room temperature for 40 min, and then alkylated with 40 mmol L^{-1} iodoacetamide (IAA, Sigma-Aldrich, USA) in the dark for 30 min. The mixture was diluted to a final concentration of 2 mol L^{-1} urea in 100 mmol L^{-1} Tris-HCl buffer for subsequent protease digestion. A total of 1 μg LysC-trypsin protease (MS grade, Thermo Fisher Scientific, USA) was added and incubated at 37°C for 16 h. The peptide mixtures were desalted using an SPE C_{18} column (SOLAμ™ Thermo Fisher Scientific, USA) and evaporated using a vacuum concentrator (Labconco, USA). The peptide samples were reconstituted in water containing 0.1% formic acid, and the phosphopeptides were enriched using a High-Select™ Fe-NTA kit (Thermo Fisher Scientific, USA) for LC-MS/MS analysis.

A nanoElute LC (Bruker Daltonics) coupled to a trapped ion mobility time-of-flight MS (timsTOF MS, Bruker Daltonics) was employed for phosphorylation identification. A ReproSil-Pur 120 C_{18} column (7.5 μm (i.d.) × 25 cm (length), 1.9 μm (particle size)) was packed for the LC separation, and the column temperature was maintained at 50°C. The mobile phases A and B were water and acetonitrile containing 0.1% formic acid, respectively. The flow rate was 300 nL min^{-1}, and the elution gradient was set as follows: 0–90 min = 2% B to 22% B, 90–100 min = 22% B to 37% B, 100–110 min = 37% B to 90% B, and 110–120 min = 90% B. The eluates were introduced to the high-resolution MS via a positive nano-ESI CaptiveSpray ion source operating in data-dependent acquisition (DDA) coupled with parallel accumulation-serial fragmentation (PASEF) mode. The capillary voltage was set as 1,500 V. The mass spectra were

recorded from 100 to 1700 m/z, the ion mobility (1/K0) from 0.6 to 1.6 V s cm^{-2}, and the collision energy linearly from 20 to 59 eV. The dual TIMS analyzer was operated at a locked duty cycle of 100% using equal accumulation and ramp times of 100 ms each, comprising one full TIMS-MS scan and ten PASEF MS/MS scans.

All DDA-PASEF raw files were analyzed using the PEAKS Online (Bioinformatics Solutions Inc., Canada) platform with a threshold control of 1% false discovery rate at the peptide-spectrum match (PSM), peptide, and protein levels. The maximum mass deviations of the parent and fragment ions were set to 15 ppm and 0.05 Da, respectively. Carbamidomethyl was set as the fixed modification, while oxidation and PTM of phosphorylation (+79.9663 Da) on Ser/Thr/Tyr residues were set as variable modifications. The MS/MS spectra were manually checked to confirm the exact phosphorylated sites according to the b- or y-characteristic fragments.

Thermostability assay

The thermostability of SARS-CoV-2 soluble ORF9b and SARS-CoV-2 refolded ORF9b, three mutants, and SARS-CoV-2 refolded ORF9b with MG (16:0) was evaluated with an all-in-one Uncle stability platform (Unchained Labs, Norton, MA, USA). The fluorescence spectrum was used to monitor the evolution of protein domain unfolding when temperature increases at a rate of 0.9°C min from 25°C to 95°C at a protein concentration of 4.5 mg mL^{-1} or 3.5 mg mL^{-1}. Label-free fluorescence from intrinsic aromatic amino acid residues excited by an excitation wavelength of 266 nm was collected for melting temperature calculations.

Data availability

Atomic coordinates and structure factors have been deposited in the protein data bank (PDB) with accession codes 7YE7 and 7YE8.

References

Adams, P.D., Afonine, P.V., Bunkóczi, G., Chen, V.B., Davis, I.W., Echols, N., Headd, J.J., Hung, L.W., Kapral, G.J., Grosse-Kunstleve, R.W., et al. (2010). *PHENIX*: a comprehensive Python-based system for macromolecular structure solution. Acta Crystlogr D Biol Crystlogr 66, 213–221.

Ajaz, S., McPhail, M.J., Singh, K.K., Mujib, S., Trovato, F.M., Napoli, S., and Agarwal, K. (2021). Mitochondrial metabolic manipulation by SARS-CoV-2 in peripheral blood mononuclear cells of patients with COVID-19. Am J Physiol-Cell Physiol 320, C57–C65.

Bai, C., Zhong, Q., and Gao, G.F. (2022). Overview of SARS-CoV-2 genome-encoded proteins. Sci China Life Sci 65, 280–294.

Blanco-Melo, D., Nilsson-Payant, B.E., Liu, W.C., Uhl, S., Hoagland, D., Møller, R., Jordan, T.X., Oishi, K., Panis, M., Sachs, D., et al. (2020). Imbalanced host response to SARS-CoV-2 drives development of COVID-19. Cell 181, 1036–1045.e9.

Bojkova, D., Klann, K., Koch, B., Widera, M., Krause, D., Ciesek, S., Cinatl, J., and Münch, C. (2020). Proteomics of SARS-CoV-2-infected host cells reveals therapy targets. Nature 583, 469–472.

Bouhaddou, M., Memon, D., Meyer, B., White, K.M., Rezelj, V.V., Correa Marrero, M., Polacco, B.J., Melnyk, J.E., Ulferts, S., Kaake, R.M., et al. (2020). The global phosphorylation landscape of SARS-CoV-2 infection. Cell 182, 685–712.e19.

Brandherm, L., Kobaš, A.M., Klöhn, M., Brüggemann, Y., Pfaender, S., Rassow, J., and Kreimendahl, S. (2021). Phosphorylation of SARS-CoV-2 Orf9b regulates its targeting to two binding sites in TOM70 and recruitment of Hsp90. Int J Mol Sci 22, 9233.

Chen, V.B., Arendall Iii, W.B., Headd, J.J., Keedy, D.A., Immormino, R. M., Kapral, G.J., Murray, L.W., Richardson, J.S., and Richardson, D.C. (2010). *MolProbity*: all-atom structure validation for macromolecular crystallography. Acta Crystlogr D Biol Crystlogr 66, 12–21.

Emsley, P., and Cowtan, K. (2004). *Coot*: model-building tools for molecular graphics. Acta Crystlogr D Biol Crystlogr 60, 2126–2132.

Gallarate, M., Trotta, M., Battaglia, L., and Chirio, D. (2009). Preparation of solid lipid nanoparticles from W/O/W emulsions: preliminary studies on insulin encapsulation. J Microencapsul 26, 394–402.

Gao, X., Zhu, K., Qin, B., Olieric, V., Wang, M., and Cui, S. (2021). Crystal structure of SARS-CoV-2 Orf9b in complex with human TOM70 suggests unusual virus-host interactions. Nat Commun 12, 2843.

Gordon, D.E., Hiatt, J., Bouhaddou, M., Rezelj, V.V., Ulferts, S., Braberg, H., Jureka, A.S., Obernier, K., Guo, J.Z., Batra, J., et al. (2020a). Comparative host-coronavirus protein interaction networks reveal pan-viral disease mechanisms. Science 370, eabe9403.

Gordon, D.E., Jang, G.M., Bouhaddou, M., Xu, J., Obernier, K., White, K. M., O'Meara, M.J., Rezelj, V.V., Guo, J.Z., Swaney, D.L., et al. (2020b). A SARS-CoV-2 protein interaction map reveals targets for drug repurposing. Nature 583, 459–468.

Jiang, H.W., Li, Y., Zhang, H.N., Wang, W., Yang, X., Qi, H., Li, H., Men, D., Zhou, J., and Tao, S.C. (2020a). SARS-CoV-2 proteome microarray for global profiling of COVID-19 specific IgG and IgM responses. Nat Commun 11, 3581.

Jiang, H.W., Zhang, H.N., Meng, Q.F., Xie, J., Li, Y., Chen, H., Zheng, Y. X., Wang, X.N., Qi, H., Zhang, J., et al. (2020b). SARS-CoV-2 Orf9b suppresses type I interferon responses by targeting TOM70. Cell Mol Immunol 17, 998–1000.

Kreimendahl, S., and Rassow, J. (2020). The mitochondrial outer membrane protein Tom70-mediator in protein traffic, membrane contact sites and innate immunity. Int J Mol Sci 21, 7262.

Krissinel, E., and Henrick, K. (2007). Inference of macromolecular assemblies from crystalline state. J Mol Biol 372, 774–797.

Lee, J.G., Huang, W., Lee, H., van de Leemput, J., Kane, M.A., and Han, Z. (2021). Characterization of SARS-CoV-2 proteins reveals Orf6 pathogenicity, subcellular localization, host interactions and attenuation by Selinexor. Cell Biosci 11, 58.

Li, H., Zhou, M., Han, J., Zhu, X., Dong, T., Gao, G.F., and Tien, P. (2005). Generation of murine CTL by a hepatitis B virus-specific peptide and evaluation of the adjuvant effect of heat shock protein glycoprotein 96 and its terminal fragments. J Immunol 174, 195–204.

Li, S., Wang, L., Li, N., Liu, Y., and Su, H. (2017). Combination lung cancer chemotherapy: design of a pH-sensitive transferrin-PEG-Hz-

lipid conjugate for the co-delivery of docetaxel and baicalin. Biomed Pharmacother 95, 548–555.

Li, Y., Xu, Z., Lei, Q., Lai, D.Y., Hou, H., Jiang, H.W., Zheng, Y.X., Wang, X.N., Wu, J., Ma, M.L., et al. (2021). Antibody landscape against SARS-CoV-2 reveals significant differences between non-structural/accessory and structural proteins. Cell Rep 36, 109391.

Liu, X.Y., Wei, B., Shi, H.X., Shan, Y.F., and Wang, C. (2010). Tom70 mediates activation of interferon regulatory factor 3 on mitochondria. Cell Res 20, 994–1011.

Lu, R., Zhao, X., Li, J., Niu, P., Yang, B., Wu, H., Wang, W., Song, H., Huang, B., Zhu, N., et al. (2020). Genomic characterisation and epidemiology of 2019 novel coronavirus: implications for virus origins and receptor binding. Lancet 395, 565–574.

Luo, Y., Yan, A., Liu, F., and Wan, Y. (2021). Analysis of three emulsifiers of glyceryl in the milk by gas chromatography-mass spectrometry. J Analyt Sci 37, 183–187.

McCallum, M., Bassi, J., De Marco, A., Chen, A., Walls, A.C., Di Iulio, J., Tortorici, M.A., Navarro, M.J., Silacci-Fregni, C., Saliba, C., et al. (2021). SARS-CoV-2 immune evasion by the B.1.427/B.1.429 variant of concern. Science 373, 648–654.

Meier, C., Aricescu, A.R., Assenberg, R., Aplin, R.T., Gilbert, R.J.C., Grimes, J.M., and Stuart, D.I. (2006). The crystal structure of ORF-9b, a lipid binding protein from the SARS coronavirus. Structure 14, 1157–1165.

Otwinowski, Z., and Minor, W. (1997). Processing of X-ray diffraction data collected in oscillation mode. Methods Enzymol 276, 307–326.

Porter, L.L., and Looger, L.L. (2018). Extant fold-switching proteins are widespread. Proc Natl Acad Sci USA 115, 5968–5973.

Qiu, M., Shi, Y., Guo, Z., Chen, Z., He, R., Chen, R., Zhou, D., Dai, E., Wang, X., Si, B., et al. (2005). Antibody responses to individual proteins of SARS coronavirus and their neutralization activities. Microbes Infect 7, 882–889.

Read, R.J. (2001). Pushing the boundaries of molecular replacement with maximum likelihood. Acta Crystlogr D Biol Crystlogr 57, 1373–1382.

Schmidt, T.G.M., Batz, L., Bonet, L., Carl, U., Holzapfel, G., Kiem, K., Matulewicz, K., Niermeier, D., Schuchardt, I., and Stanar, K. (2013). Development of the Twin-Strep-tag® and its application for purification of recombinant proteins from cell culture supernatants. Protein Expr Purif 92, 54–61.

Song, H., Qi, J., Haywood, J., Shi, Y., and Gao, G.F. (2016). Zika virus NS1 structure reveals diversity of electrostatic surfaces among flaviviruses. Nat Struct Mol Biol 23, 456–458.

Thorne, L.G., Bouhaddou, M., Reuschl, A.K., Zuliani-Alvarez, L., Polacco, B., Pelin, A., Batra, J., Whelan, M.V.X., Hosmillo, M., Fossati, A., et al. (2022). Evolution of enhanced innate immune evasion by SARS-CoV-2. Nature 602, 487–495.

Tian, M., Chen, M., Bao, Y.L., Xu, C.D., Qin, Q.Z., Zhang, W.X., He, Y.T., and Shao, Q. (2017). Sputum metabolomic profiling of bronchial asthma based on quadruple time-of-flight mass spectrometry. Int J Clin Exp Pathol 10, 10363–10373.

Tian, W., Li, D., Zhang, N., Bai, G., Yuan, K., Xiao, H., Gao, F., Chen, Y., Wong, C.C.L., and Gao, G.F. (2021). O-glycosylation pattern of the SARS-CoV-2 spike protein reveals an "O-Follow-N" rule. Cell Res 31, 1123–1125.

Tian, W., Zhang, N., Jin, R., Feng, Y., Wang, S., Gao, S., Gao, R., Wu, G., Tian, D., Tan, W., et al. (2020). Immune suppression in the early stage of COVID-19 disease. Nat Commun 11, 5859.

Trivino, A., Gumireddy, A., and Chauhan, H. (2019). Drug-lipid-surfactant miscibility for the development of solid lipid nanoparticles. AAPS PharmSciTech 20, 46.

Truzzi, E., Bongio, C., Sacchetti, F., Maretti, E., Montanari, M., Iannuccelli, V., Vismara, E., and Leo, E. (2017). Self-assembled lipid nanoparticles for oral delivery of heparin-coated iron oxide nanoparticles for theranostic purposes. Molecules 22, 963.

Wu, F., Zhao, S., Yu, B., Chen, Y.M., Wang, W., Song, Z.G., Hu, Y., Tao, Z.W., Tian, J.H., Pei, Y.Y., et al. (2020). Author correction: a new coronavirus associated with human respiratory disease in China. Nature 580, E7.

Xu, K., Zheng, B.J., Zeng, R., Lu, W., Lin, Y.P., Xue, L., Li, L., Yang, L.L., Xu, C., Dai, J., et al. (2009). Severe acute respiratory syndrome coronavirus accessory protein 9b is a virion-associated protein. Virology 388, 279–285.

Yang, J., Zhang, G., Yu, D., Cao, R., Wu, X., Ling, Y., Pan, Y.H., Yi, C., Sun, X., Sun, B., et al. (2021). A Kozak-related non-coding deletion effectively increases B.1.1.7 transmissibility. bioRxiv: 2021.04.30.442029v2.

Zhang, J., Xiao, T., Cai, Y., Lavine, C.L., Peng, H., Zhu, H., Anand, K., Tong, P., Gautam, A., Mayer, M.L., et al. (2021). Membrane fusion and immune evasion by the spike protein of SARS-CoV-2 Delta variant. Science 374, 1353–1360.

Zhu, N., Zhang, D., Wang, W., Li, X., Yang, B., Song, J., Zhao, X., Huang, B., Shi, W., Lu, R., et al. (2020). A novel coronavirus from patients with pneumonia in China, 2019. N Engl J Med 382, 727–733.

SUPPORTING INFORMATION

The supporting information is available online at https://doi.org/10.1007/s11427-022-2168-8. The supporting materials are published as submitted, without typesetting or editing. The responsibility for scientific accuracy and content remains entirely with the authors.